ARTICLE

Computational Approach for Automated Segmentation and Classification of Region of Interest in Lateral Breast Thermograms

Dennies Tsietso[1,*], Abid Yahya[1], Ravi Samikannu[1], Basit Qureshi[2] and Muhammad Babar[3,*]

[1]Department of Electrical, Computer and Telecommunications Engineering, Botswana International University of Science and Technology, Palapye, Private Bag 16, Botswana

[2]College of Computer and Information Sciences, Prince Sultan University, Riyadh, 11586, Saudi Arabia

[3]Robotics and Internet of Things Lab, Prince Sultan University, Riyadh, 11586, Saudi Arabia

*Corresponding Authors: Dennies Tsietso. Email: dennies.tsietso@studentmail.biust.ac.bw; Muhammad Babar. Email: mbabar@psu.edu.sa

ABSTRACT

Breast cancer is one of the major health issues with high mortality rates and a substantial impact on patients and healthcare systems worldwide. Various Computer-Aided Diagnosis (CAD) tools, based on breast thermograms, have been developed for early detection of this disease. However, accurately segmenting the Region of Interest (ROI) from thermograms remains challenging. This paper presents an approach that leverages image acquisition protocol parameters to identify the lateral breast region and estimate its bottom boundary using a second-degree polynomial. The proposed method demonstrated high efficacy, achieving an impressive Jaccard coefficient of 86% and a Dice index of 92% when evaluated against manually created ground truths. Textural features were extracted from each view's ROI, with significant features selected via Mutual Information for training Multi-Layer Perceptron (MLP) and K-Nearest Neighbors (KNN) classifiers. Our findings revealed that the MLP classifier outperformed the KNN, achieving an accuracy of 86%, a specificity of 100%, and an Area Under the Curve (AUC) of 0.85. The consistency of the method across both sides of the breast suggests its viability as an auto-segmentation tool. Furthermore, the classification results suggests that lateral views of breast thermograms harbor valuable features that can significantly aid in the early detection of breast cancer.

KEYWORDS

Breast cancer; CAD; machine learning; ROI; segmentation; thermography

1 Introduction

Breast Cancer is one of the most fatal diseases globally. As per 2020 Global Cancer Observatory (GLOBOCAN) statistics, there were 2.3 million registered cases and 685,000 were fatal,which made it the second most common cause of death among women [1]. In developed countries, the incidence rate is higher than in developing countries [2,3]. Cancer is characterized by uncontrolled cell proliferation [4,5], and if the cells invade other body parts, it is classified as invasive; otherwise, it is categorized as non-invasive [6]. Identifying cancer early on effectively prevents aggressive treatments such as

mastectomy [7]. Generally, early detection is conducted through mammography. However, this invasive procedure causes discomfort and uses an ionizing radiation dose, which increases the chances of developing radiation-induced breast cancer [8]. On the contrary, thermography is an economical, radiation-free, and noninvasive screening modality that can also be used, particularly for dense breasts [9]. This approach relies on the observation that the human body exhibits a level of thermal symmetry when in a healthy state. Otherwise, it is abnormal. This anomaly signifies a higher metabolic activity, possibly due to cancerous cells [10].

Thermography measures the surface temperature of the breasts. These temperature variations are visualized as color-coded maps called thermograms. Analysis involves comparing the temperature distribution between corresponding regions (contralateral breasts) for abnormalities. To facilitate this comparison, segmentation techniques are used to isolate the Region of Interest (ROI) from the thermogram. While various methods exist for segmenting frontal view thermograms, which capture a larger portion of the breast, there's a gap in techniques for segmenting lateral view thermograms. These side-view images hold valuable information for detecting tumors in the lateral breast tissue. Accurate segmentation of both frontal and lateral views is crucial for developing robust Computer-Aided Detection (CAD) systems. Successful CAD systems can potentially reduce workload for pathologists and minimize subjectivity in breast cancer diagnoses [11].

This paper proposes a novel technique for segmenting lateral-view breast thermograms. The method extracts texture features from the segmented ROIs. A subset of these features is then used to train a machine learning algorithm to differentiate between healthy and cancerous thermograms. We evaluated our approach using a dataset of 31 healthy and 26 cancerous subjects acquired with the Static Infrared Thermography (SIT) protocol at a 90-degree angle. The main contributions of this paper are twofold:

- We propose a novel technique for segmenting lateral-view breast thermograms. This fills a critical gap in current methods that focus mainly on frontal views. By including the sides of the breast, where tumors can also arise, our segmentation approach has the potential to improve breast cancer detection in thermography
- We explore the feasibility of using machine learning for breast cancer classification based on the segmented lateral-view thermograms

The rest of the article has been structured in the following manner: Section 2 outlines the related works on breast cancer detection; Section 3 details our methods and the data set used for the experiment. The experimental results are explored in depth in Section 4 and discussed further in Section 5 before all is wrapped up with the conclusion provided in Section 6.

2 Related Work

Research has recently been devoted to breast thermography. For example, in [12], fuzzy active contours were employed to segment cancerous tissue regions on frontal and lateral breast thermograms. The segmentation results were validated with manually segmented ground truths. The method achieved 91.98% accuracy 85% sensitivity. Madhavi et al. [13] presented a multi-view breast thermogram analysis by textural feature fusion. The level-set method was used for segmenting lateral breast thermograms in their method. Rather than periodically resetting the level set function to its initial state for controlling numerical errors, they employed the level set evolution without re-initialization. Gray-Level Co-occurrence Matrix (GLCM) features were independently extracted from the frontal, left-lateral, and right-lateral thermograms. Feature fusion was undertaken on the extracted lateral

and frontal ROIs to create a composite feature vector. Fused textures achieved 96% accuracy, 92% specificity, and 100% sensitivity.

In Reference [14], a segmentation approach was proposed to consider spatial information pixels in breast thermograms. The approach employed a metaheuristic algorithm referred to as the Dragonfly Algorithm (DA) to seek out the most suitable threshold values for dividing a breast thermogram into distinct regions that are homogeneous and well-defined. This was applied to the image's energy curve. The DA was evaluated using Kapur and Otsu as objective functions and was found to iterate until it reached an optimal solution. Moreover, four optimization algorithms were applied to the Otsu and Kapur functions and compared with the DA over eight randomly chosen breast thermograms, including lateral views. The DA achieved superior performance compared to other implementations for Otsu and Kapur variants across most metrics, producing thermograms with clear borders.

Kapoor et al. [15] introduced an approach for the automatic segmentation ROI from breast thermograms and analyzing breast thermogram asymmetry to classify a breast as healthy or abnormal. The undesirable body part, which included the waistlines and shoulder region, was initially cropped away to identify the breast limits. The Canny edge detector was then employed to detect edges, and to estimate bottom breast boundary curves. After decimating the area below the bottom boundaries, the remaining region was separated into the left and right breasts. Histograms were created, and features were extracted from each side to analyze the asymmetry of the contralateral breasts. We concur with asymmetry analysis, as it can serve as a second set of eyes for diagnostics.

Venkatachalam et al. [16] presented a segmentation technique resilient to impediments normally encountered in breast thermogram datasets, including low contrast, a low signal-to-noise ratio, and overlapping ROIs. The approach employs the active contour method to segment the ROI affected by inflammation. Initially, the inflamed ROI is localized, and active contours are automatically initialized based on the multi-scale local and global fitted image models. The method's validity was assessed by comparing its output with ground truths generated by an expert. Their method was resilient against breast thermograms' severe intensity inhomogeneity and could precisely segment the inflamed ROI. Moreover, second-order statistical descriptors were extracted from the ROIs to classify the images as malignant or benign. The technique was evaluated on two datasets and compared to existing state-of-the-art methods such as fuzzy C-means, K-means, and Chan-Vese, all of which it outperformed in accuracy.

3 Materials and Methods

This section details a fully automatic approach for segmenting the ROI from lateral breast thermograms. We begin by outlining the characteristics of the thermogram dataset used in the study. The segmentation process itself follows a multi-step approach. First, the thermal images undergo denoising to remove unwanted noise before edge detection. Morphological operations are then applied to enhance the extracted edges. Subsequently, the approach leverages information from the image acquisition protocol to identify crucial areas for isolating the breast boundary. Utilizing the bottom boundary points, the entire boundary is then estimated. Finally, a binary mask is generated based on the segmented ROI and overlaid onto the original thermogram to create the final ROI image.

3.1 Dataset

This study utilized thermograms from the Database for Mastology Research (DMR). This publicly accessible database with thermograms was acquired from volunteers by Federal Fluminense University in Brazil [17]. It hosts images acquired from numerous views via the Static Infrared

Thermography and Dynamic Infrared Thermography (DIT) protocols. For acquisition, a FLIR SC-620 thermal infrared camera with a resolution of 640×480 pixels and a thermal sensitivity of 40 mK. This work used a sample of 101 lateral thermograms (75 normal, 26 abnormal) captured at 90 degrees angle using the SIT protocol. We selected the DMR dataset because its metadata includes comprehensive details about how the thermograms were acquired. This rich metadata is vital for ensuring the reproducibility of our segmentation method. In other words, our method can be applied to any thermograms acquired using the same protocols as the DMR dataset. Additionally, unlike some datasets focused on specific demographics, DMR includes thermograms from a broader patient population. This variety in breast shapes and sizes is essential for developing a generalizable segmentation method applicable to a diverse patient base.

3.2 Segmentation

3.2.1 Preprocessing

Before removing the breast boundary from undesirable areas, such as the neck and back. The thermogram was converted to grayscale and denoised with a Gaussian kernel. This filter was adopted for its simplicity and robustness against noise [18]. In image processing, a two-dimensional variant of the Gaussian function is used, as defined in Eq. (1).

$$F(u, v) = \frac{1}{2\pi\sigma^2} \exp\left(-\frac{u^2 + v^2}{2\sigma^2}\right) \tag{1}$$

where σ is the standard deviation of the Gaussian kernel, and u and v are the respective distances to the horizontal and vertical centers of the kernel. The Gaussian smoothed image I_s is obtained by convolving the grayscale image $I(u, v)$ with a two-dimensional Gaussian filter, $I_s = F_\sigma \circledast I$. This work set a Gaussian kernel to $\sigma = 1.618$ balancing noise reduction with edge preservation.

3.2.2 Breast Boundary Extraction

The extraction of the bounding rectangle encompassing the breast region was accomplished by leveraging a gradient image, which was a guiding mechanism for the extraction procedure. A Canny edge detector was used to detect edges in the denoised image. This algorithm detects abrupt changes in image intensity in a small region. It employs a convolution gradient operator to magnify regions with high spatial derivatives to compute image gradient magnitude at each pixel as $||\nabla F_\sigma \circledast I||$. The gradient orientation is then determined at each pixel using Eq. (2).

$$\hat{d} = \frac{\nabla F_\sigma \circledast I}{||\nabla F_\sigma \circledast I||} \tag{2}$$

Non-border pixels are then suppressed via non-maxima suppression. Finally, hysteresis thresholding is used to identify weak and strong edges based on a threshold. This detector is recognized as the best edge detector due to its superior localization and noise resilience [19], hence its wide adoption in image processing. A threshold of $\alpha = 0.233$ was found to produce the desired edges and was utilized across all images. Fig. 1 demonstrates the application of the Canny edge detector on grayscale images of lateral breast thermograms. Fig. 1a shows the original grayscale images, while Fig. 1b presents the gradient images post edge detection. Accurate edge detection ensures precise delineation of the breast region, minimizing noise and irrelevant data, which is essential for isolating the ROI. The detected edges are a foundation for further morphological operations and subsequent analysis steps, contributing to the method's robustness and consistency. While Canny edge detection

offers robust performance, exploring alternative edge detectors with less parameter sensitivity such as deep learning-based edge detection methods could be a future investigation.
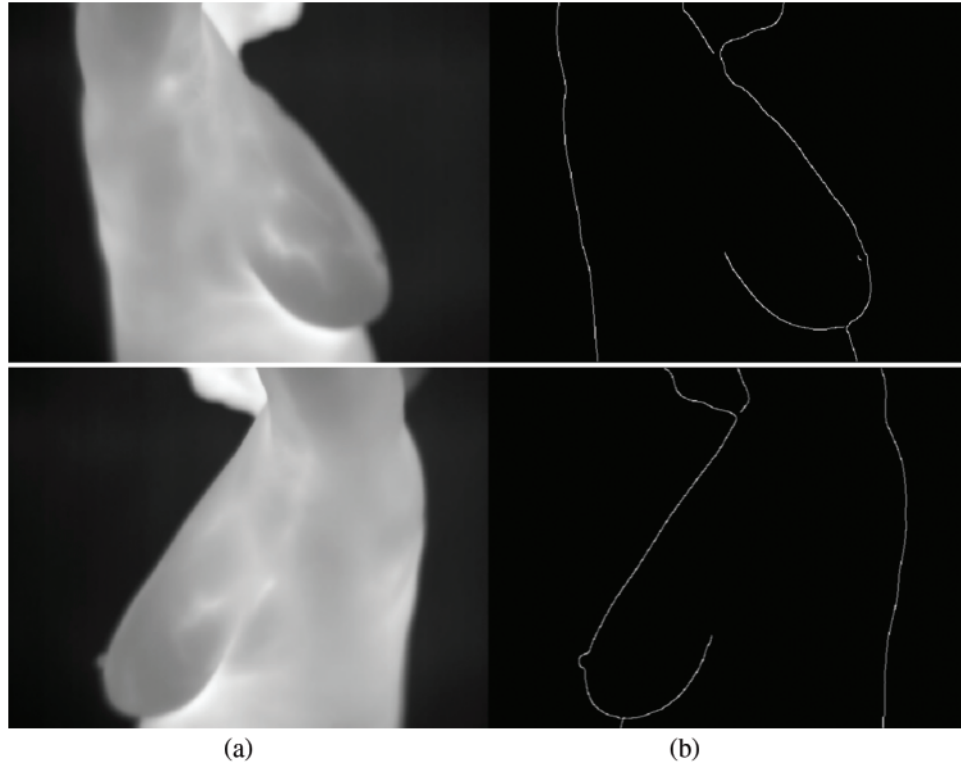
Figure 1: Edges generated by the Canny edge detector. (a) Grayscale images. (b) Gradient image

The morphological operations of closing and dilation were employed to connect disconnected boundaries and enhance the overall boundary. These operations are described in Eqs. (3) and (4).

$$I \cdot S = (I \oplus S) \ominus S \tag{3}$$

$$I \circ S = (I \ominus S) \oplus S \tag{4}$$

where I denotes the gradient image and S is the structuring element. A 3×3 structuring element was employed for morphological closing and dilation operations. This size was effectively connecting small gaps in the boundaries while minimizing unintended modifications. Exploring adaptive structuring element selection based on image features might be an avenue for further improvement. To filter out the armpit area and an area above it, as shown in Fig. 2, the row y_n and column x_n of the convex point formed by the neck and chest area were used as coordinates for decimating the unwanted area. For the right breast, all objects below this column and its row were removed from the original edge image, and vice versa for the left side view, leaving only the breast boundary.

3.2.3 Polynomial Curve Fitting

The bottom breast boundary was traced and fitted to a second-degree polynomial to estimate the bottom boundary curve, as shown in Fig. 3a. Finally, the intersection points of the curve and boundary points were calculated and marked, as illustrated in Fig. 3b.

(a)

(b)
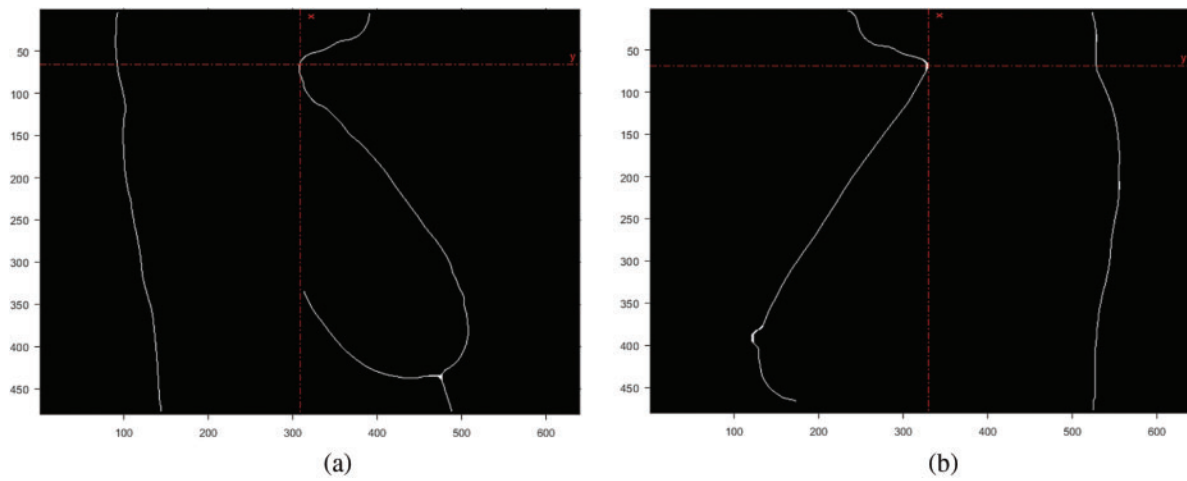
Figure 2: Coordinate for the convex point of the neck area. (a) Right breast. (b) Left breast

(a)

(b)
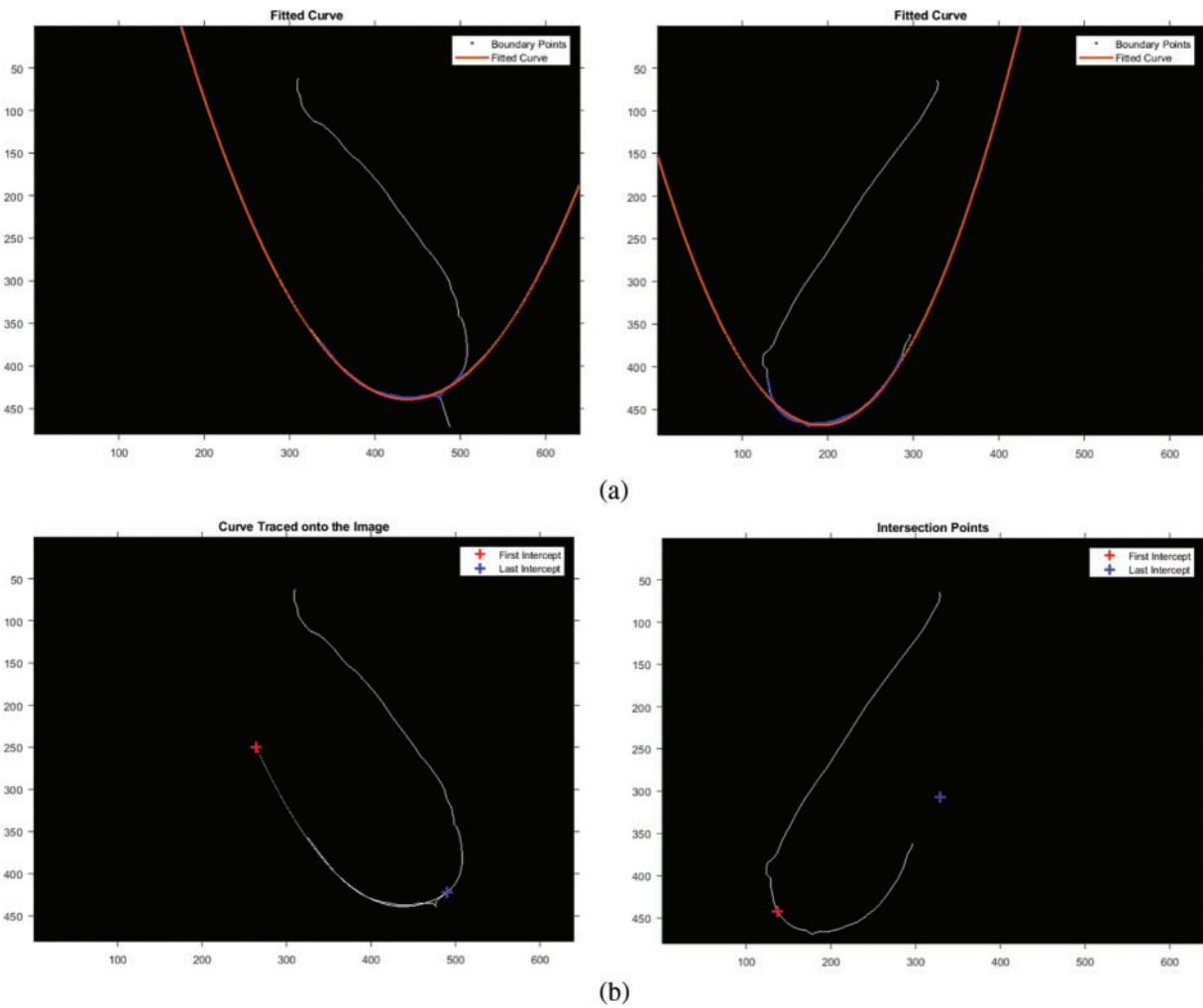
Figure 3: (Continued)

(c)
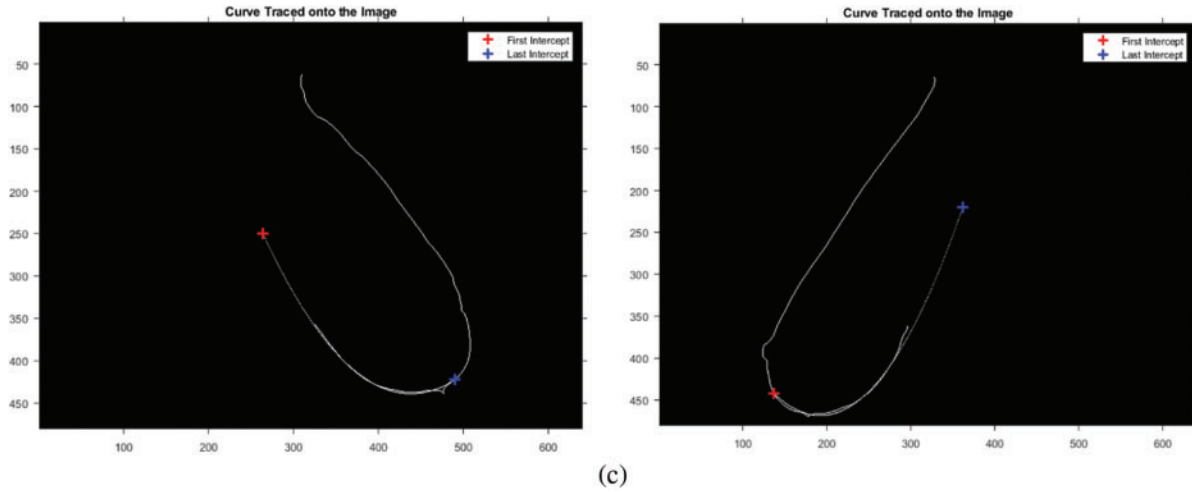
Figure 3: Estimation of the bottom breast boundary. (a) Fitted curve. (b) Intersection points. (c) Intersection points after rotation

The dataset contains images of different breast structures; to preserve data across all ROIs, the intersection of the boundary column x_n and the curve (x_{interA}, y_{interA}) was rotated about point (x_n, y_n). For the right breast, the point was shifted to -15 degrees, and vice versa for the other side. Finally, we computed the intersection of the fitted curve and the new line that crosses the curve to obtain (x_{interB}, y_{interB}); the curve was then engraved onto the image, as shown in Fig. 3c.

3.2.4 Mask and Region of Interest Generation

After engraving the curve onto the image, a straight line was drawn from (x_n, y_n) to (x_{interB}, y_{interB}) to close the breast boundary. Morphological closing and dilation operations succeeded in closing the boundary completely. Ultimately, an image fill operation was employed to populate the identified breast region with white pixels, creating a mask. This mask was subsequently overlaid onto the original image, creating an ROI as illustrated in Fig. 4.

The segmentation steps for the right-side thermogram can be summarized as follows:

1. Read a grayscale image I_g and find gradient image I_e with the Canny edge detector as shown in Fig. 1
2. Identify the coordinates (x_n, y_n) for the convex point formed by the neck and chest area as illustrated in Fig. 2 and decimate everything outside that area to form the breast boundary I_b
3. To locate the bottom breast boundary, from I_b, locate point (x_t, y_t) which defines the start point of the inframammary folds
4. Trace the boundary of points bounded by coordinates (x_t, y_t) and find the first pixel for each column. This results in the bottom boundary points (X_{bottom}, Y_{bottom})
5. Fit a second-degree polynomial to the points (X_{bottom}, Y_{bottom}) and determine the left $L = (x_{interA}, y_{interA})$ and right R intersection points of this curve with column x and x_t as shown in Fig. 3b
6. Rotate the left intersection point $(L = x_{interA}, y_{interA})$ -15 degrees about point (x_n, y_n) and define the new point $L = (x_{interB}, y_{interB})$ as the intersection of a straight line from (x_n, y_n) with the curve
7. Engrave the curve onto the image I_e along with the straight line from (x_n, y_n) to form I_{eng}
8. Perform morphological closing, dilation and imfill to form a ROI mask, as depicted in Fig. 4
9. Impose the mask onto the original image to form a ROI image

The same steps were used for the left-side segmentation but considering some coordinates opposite the right-side view.

(a)　　　　　　　　　　　　　　　　(b)
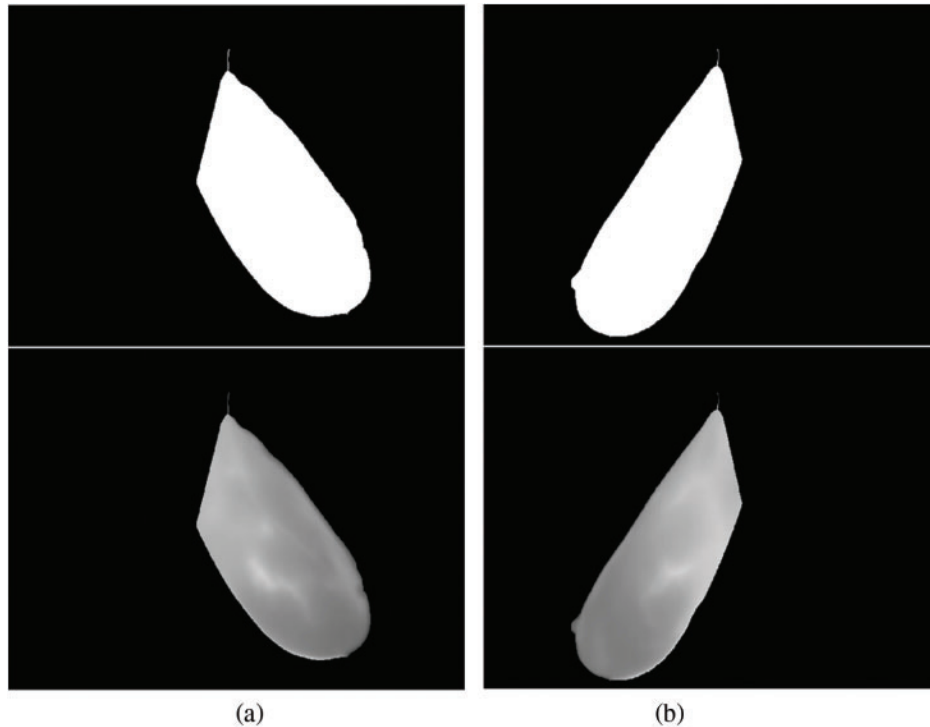
Figure 4: Generated binary masks and ROI for: (a) the right breast; (b) left breast

3.3 Feature Extraction

3.3.1 Textural Feature Extraction

Texture, which characterizes the spatial organization of pixel values, plays a vital role in thermal image analysis for breast cancer detection, as it can reveal important information about disease progression [20]. The Gray Level Co-occurrence Matrix (GLCM) technique considers the spatial relationship between pixel intensities [21]. It generates a feature matrix describing the image's texture. In this study, 26 distinct GLCM features were derived from each ROI of breast thermograms. These features, such as contrast, homogeneity, cluster shade, sum entropy, sum variance, and difference entropy, were extracted to capture the complexity and heterogeneity of breast tissue, which is crucial for cancer detection [22].

3.3.2 Feature Selection

The Mutual Information (MI) approach was employed for feature selection. This technique quantifies how well a feature distinguishes between healthy and malignant cases, thus helping to identify features with low discriminative power. By eliminating these uninformative features, this can reduce the dimensionality of the feature space, potentially improving classifier performance [23]. The feature selection was performed independently for both left and right lateral thermograms using a threshold value of $th = 0.05$. This threshold helped eliminate features with low relevance for cancer classification. The remaining informative features were then combined to form a composite

feature vector, capturing the salient characteristics of both breasts. This approach resulted in a highly informative feature set.

3.4 Classifier

To detect breast cancer, we trained two binary classifiers: a K-Nearest Neighbors (KNN) and a Multi-Layer Perceptron (MLP). These classifiers were trained on a composite feature vector, which combined textural, morphological, and statistical features extracted from the left and right breast ROIs. To optimize classifier performance, we employed a 10-fold cross-validation process on the training set (80% of the data). Hyperparameters, which are settings within the models, were adjusted during this process. Finally, the classifiers were evaluated on the remaining 20% of the test set. The effectiveness of the approach was assessed using various performance metrics: precision, accuracy, F1-score, recall, and Area Under the Curve (AUC). The best performing classifier's results were then compared with existing literature to evaluate its effectiveness in breast cancer detection.

4 Results

4.1 Segmentation Results

Fig. 5 depicts the patient's original breast thermograms and the ROIs segmented by the proposed method. Nevertheless, the dataset used in this work does not have ground truths for validation. As a result, they were manually created. These were used to validate the method based on two image similarity metrics: Dice Index (DI) and the Jaccard Index (JI). These are widely used metrics for validating segmentation results. They directly compare a ground truth I_{gt} and our method's ROI I_{exp}. They compute the fraction of intersecting and non-intersecting segments and ground truth. They are theoretically specified in Eqs. (5) and (6).
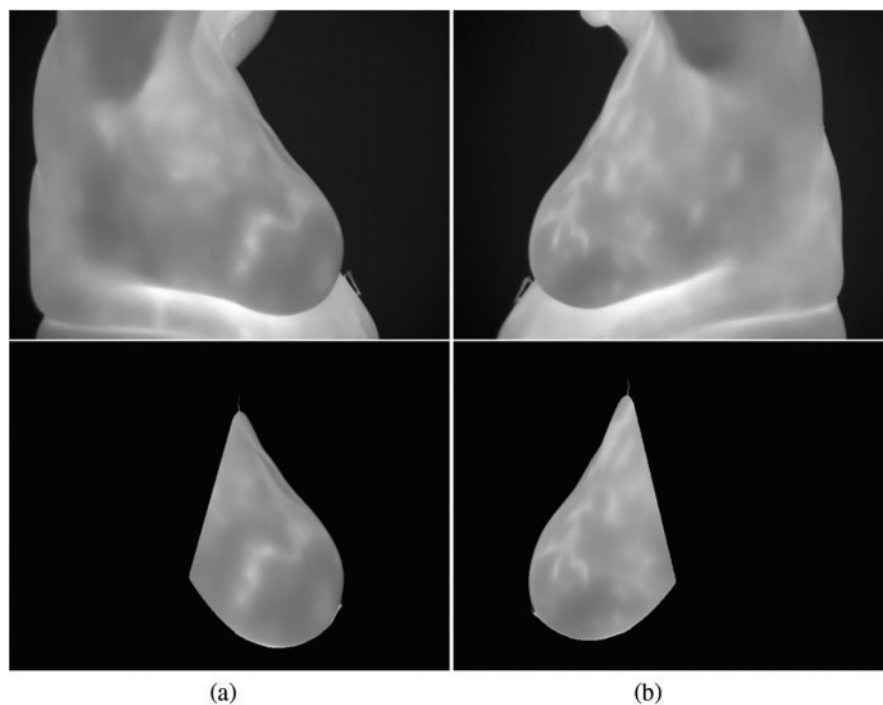

Figure 5: Segmentation results for a particular instance: (a) right breast (b) left breast

$$\textit{Jaccard Coefficient}: \; J\left(I_{gt}, I_{exp}\right) = \frac{\left|I_{gt} \cap I_{exp}\right|}{\left|I_{gt} \cup I_{exp}\right|} \tag{5}$$

$$\textit{Dice Coefficient}: \; D\left(I_{gt}, I_{exp}\right) = \frac{2\left|I_{gt} \times I_{exp}\right|}{\left|I_{gt}\right| + \left|I_{exp}\right|} \tag{6}$$

It should be noted that all of the segmented images and ground truths are compared in binary form, with white pixels representing the ROI. Fig. 6 depicts the overlap between the ground truth and the generated ROI, and the associated Jaccard and Dice scores for each case. The white region represents the True Positives (TP), the magenta region represents False Negatives (FN), the green region shows the False Positives (FP), and the black pixels for True Negatives (TN). In this instance, the TP area dominates most of the region, resulting in high Dice and Jaccard scores, signifying more similarity between the ground-truth and the segmented ROI.
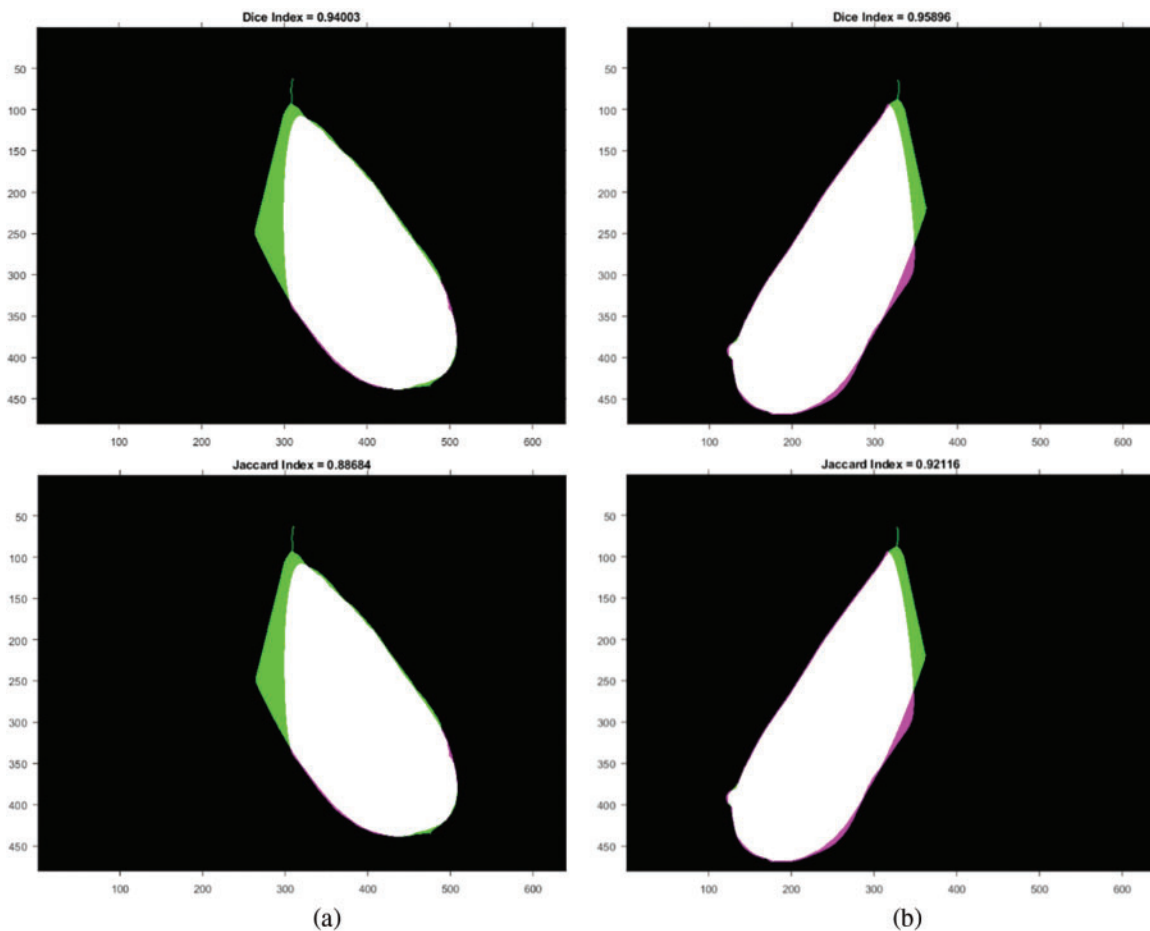
Figure 6: Similarity measures between ground-truth and generated ROI: (a) right breast and (b) left breast

The other performance metrics used in this work are sensitivity (sens), precision (prec), specificity (spec), accuracy (acc), and Matthews Correlation Coefficient (MCC), which are defined from Eqs. (7)–(12).

$$Accuracy = \frac{TP + TN}{TP + TN + FP + FN} \tag{7}$$

$$F1\ Score = \frac{2 \times TP}{2 \times TP + FP + FN} \tag{8}$$

$$Specificity = \frac{TN}{TN + FP} \tag{9}$$

$$Sensitivity = \frac{TP}{TP + FN} \tag{10}$$

$$Precision = \frac{TP}{TP + FP} \tag{11}$$

$$MCC = \frac{(TP \times TN) - (FN \times FP)}{\sqrt{(TP + FN) \times (TN + FP) \times (TP + FP) \times (TN + FN)}} \tag{12}$$

The approach maintained consistent performance across all metrics on both sides of the breast, as presented in Table 1.

Table 1: Performance of the segmentation method

Side	Jaccard index (%)	Dice index (%)	MCC
Left	87	93	0.92
Right	84	91	0.90
Avg	86	92	0.91

4.2 Classification Results

ROIs from left and right lateral view thermograms were used for feature extraction. Each lateral view yielded 26 GLCM texture features, yielding 52 features. The MI was used to perform feature selection on each view separately. As already discussed, features with MI< 0.05 were dropped leaving only the more significant ones. As seen in Table 2, this greatly reduced the feature vector to 19. Only 9 GLCM features proved superior in discriminating the healthy class from the unhealthy class in the right-view breast thermogram, whereas the left side had only 10.

Table 2: Feature selected through mutual information

Left side thermograms	Right side thermograms
Homogeneity	Kurtosis
Kurtosis	Homogeneity
Variance	Correlation
Mean	Variance
Std	Energy
Skewness	Std

(Continued)

Table 2 (continued)

| Left side thermograms	Right side thermograms
Correlation	Mean
Contrast	Skewness
Energy	Entropy
Entropy	

The composite feature vector was used to train two classifiers to detect breast cancer: MLP and a KNN. The performance results for these models are summarized in Table 3. Fig. 7 depicts their ROC curves.
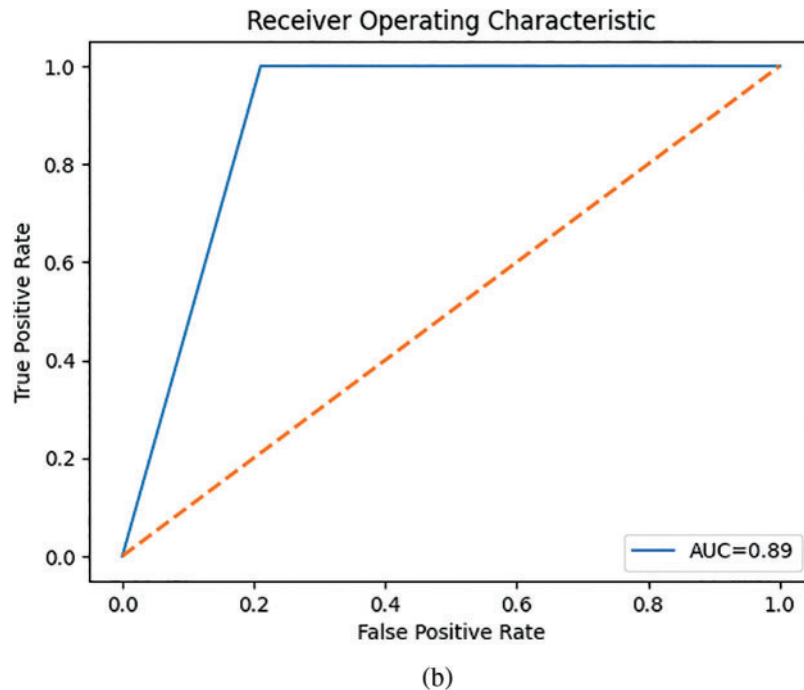
The MLP outperformed the KNN classifier.

Table 3: Performance of the segmentation method

Model	Sen. (%)	Spec. (%)	Prec. (%)	Acc. (%)	F1 score	MCC	AUROC
MLP	83	100	100	86	0.91	0.65	0.917
KNN	79	100	100	81	0.88	0.51	0.895

Note: Precision (Prec.), Sensitivity (Sen.), Accuracy (Acc.), Specificity (Spec.).

(a)
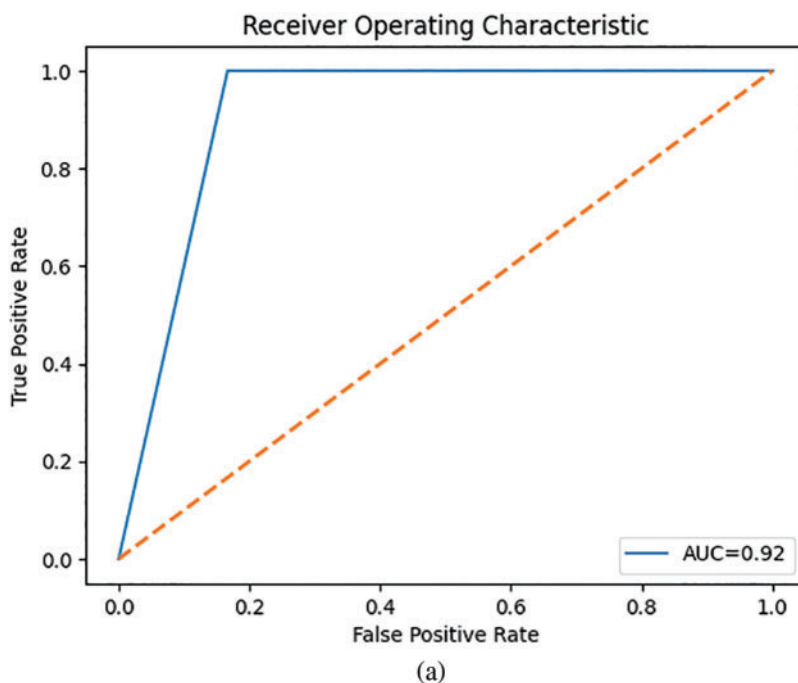
Figure 7: (Continued)

Figure 7: ROC curves for the classifiers: (a) MLP and (b) KNN

5 Discussion

In this study, we proposed a method for automatically segmenting and detecting breast cancer from lateral thermograms. First, ROIs were extracted from each image view. Then, manually generated ROIs were used to validate the auto-segmented ROIs based on image similarity metrics. The average similarity between the ground-truth and auto-segmented ROI based on the Jaccard index and Dice score was 86% and 92%, respectively. The model performed consistently on both left and right view thermograms. This is evidenced by the low standard deviation of the Jaccard index (left-side: $\sigma_{JL} = 0.07$, right-side: $\sigma_{JR} = 0.106$) and Dice score (left-side: $\sigma_{DL} = 0.045$, right-side: $\sigma_{JR} = 0.106$). These results demonstrate that the model's accuracy in segmenting the left and right view thermograms was stable across multiple instances. The observed slight differences in performance between the left and right view thermograms could be attributed to variations in the patient's orientation during acquisition.

After extracting GLCM textural descriptors from the ROIs, the MI was calculated from the GLCMs of each view. This MI helped select the most significant features for differentiating between healthy and malignant tissue. As shown in Table 2, the left view thermograms offered more distinguishing features (healthy *vs*. malignant) compared to the right view (only nine features). These informative features from both sides were then combined into a composite feature vector for training a KNN and a MLP classifier. Table 3 summarizes the performance of the KNN and MLP models on the test set. The KNN achieved a high AUC score, indicating strong performance in identifying positive cases (malignant). However, this came at the expense of a high false negative rate (i.e., low TN), meaning it missed a significant number of actual malignant cases. This could be attributed to the class imbalance in our dataset, with more malignant cases than healthy ones. The MLP, on the other hand, outperformed the KNN across all metrics.

While the MLP outperformed the KNN across all metrics, most existing investigations, as shown in Table 4, relied on GLCM features or their derivatives (i.e., Haralick features). This is likely due to the valuable information GLCM features provide about the spatial relationships between pixels in an image. It is important to note that some related works as shown in Table 4 did not mention using feature selection. This is a crucial step in machine learning, as it reduces model complexity by selecting only the most informative features. Irrelevant features can introduce noise and lead to overfitting on the training data, ultimately increasing generalization error. Additionally, hyperparameter optimization could have further improved performance. Hyperparameters are settings within the machine learning model that can significantly influence its outcome. Despite using only lateral view thermograms, our work achieved competitive results with an accuracy of 86% and an AUC of 0.92. We believe incorporating features from the corresponding frontal thermograms could further enhance these promising results.

Table 4: Comparison of the method with related works

Ref.	Descriptors	Feature selection	Size of dataset	View(s)	Model.	Sen. (%)	Spec. (%)	Prec. (%)	Acc. (%)	AUC
Ours	GLCM	MI	101 (75 healthy, 26 sick)	Left-90°, right-90°	MLP	83	100	100	86	0.92
[11]	GLCM, GLSZM, GLRLM, and NGTDM	t-test	63 (32 normal, 31 abnormal)	Front, left-90°, right-90°	LS-SVM	92	100	100	96	–
[16]	GLCM, area-based, and average intensity-based	–	100 (50 malignant, 50 benign)	Front	SVM	91	92	–	91.5	–
[24]	Haralick, Hu's moment, deviation of shape, and vascular	–	155 (81 normal, 74 abnormal)	Front	MLP	90.6	91.3	92.8	90.9	0.94
[25]	GLCM	K-means	100 (45 abnormal, 55 normal)	Front	Bayes network	95.5	100	100	98	0.99
[26]	Shape FOS, Haralick relation context	–	63 (35 normal, 28 abnormal)	Front	CNN	100	100	100	100	1
[27]	Statistical, texture and gabor	–	–	Front	SVM	95	100	–	97	–
[28]	Wavelet local energy	RSFS and GA	100 (47 abnormal, 53 normal)	Front	SVM	87	94	–	91	–

Overall, this work proposes a novel, non-invasive method for early breast cancer detection using thermography. By automating image segmentation and classification, it offers a complementary tool for clinicians. This automation can reduce manual workload, promote consistent and accurate results, and streamline the clinical workflow. The generated ROIs can allow radiologists to swiftly identify suspicious areas, thus facilitating faster and more accurate diagnoses. Additionally, these ROIs decrease the processing burden for classifiers by narrowing the analysis to relevant regions. Integration of this approach to other CAD systems can further empower radiologists, reduce their workload, and significantly improve diagnostic efficiency. Furthermore, the potential for self-screening with this technology paves the way for increased patient autonomy and earlier detection of breast cancer.

6 Conclusion

Accurate segmentation of the ROI in breast thermograms is crucial for effective breast cancer detection. However, achieving high accuracy in this process can be challenging. In this study, we proposed a polynomial fitting-based approach for extracting the ROI from both left and right lateral breast thermograms captured at a 90-degree angle. The method achieved high reliability, with an average Jaccard score of 87.2% and an average accuracy of 98.3%. Following segmentation, textural descriptors were extracted from the ROIs. Then the MI was employed to select the most relevant GLCM features for differentiating between healthy and malignant tissue. A combined feature vector comprising ten GLCM features from both left and right breasts was used to train KNN and MLP classifiers. The MLP classifier achieved promising results, demonstrating 80% specificity, 93% sensitivity, 90% accuracy, and an AUC of 0.85. Addressing the class imbalance in the dataset and incorporating features from frontal thermograms could potentially improve these results, as frontal views offer more additional information. Future work will explore the adoption of deep learning techniques, which can perform automatic feature extraction. Additionally, we aim to investigate the use of optimization algorithms to refine model performance and potentially reduce the dimensionality of the dataset.

Author Contributions: The authors confirm their contribution to the paper as follows: study conception and design: Dennies Tsietso, Muhammad Babar and Basit Qureshi; data collection: Ravi Samikannu; analysis and interpretation of results: Dennies Tsietso and Abid Yahya. All authors reviewed the results and approved the final version of the manuscript.

Availability of Data and Materials: The data that support the findings of this study are available from the corresponding author, Dennies Tsietso, upon reasonable request.

Ethics Approval: The study was conducted in accordance with the ethical principles outlined by the Botswana International University of Science and Technology and was approved by the Institution's Human Ethics Research Committee (Certificate HREC-004, dated 20/04/2022). Informed consent was obtained from all participants.

Conflicts of Interest: The authors declare that they have no conflicts of interest to report regarding the present study.

References

[1]   H. Sung *et al.*, "Global cancer statistics 2020: GLOBOCAN estimates of incidence and mortality worldwide for 36 cancers in 185 countries," *CA Cancer J. Clin.*, vol. 71, no. 3, pp. 209–249, 2021. doi: 10.3322/caac.21660.

[2]   M. Macedo, M. Santana, W. P. dos Santos, R. Menezes, and C. Bastos-Filho, "Breast cancer diagnosis using thermal image analysis: A data-driven approach based on swarm intelligence and supervised learning for optimized feature selection," *Appl. Soft Comput.*, vol. 109, Sep. 2021, Art. no. 107533. doi: 10.1016/j.asoc.2021.107533.

[3]   S. Ahmad, S. Ur Rehman, A. Iqbal, R. K. Farooq, A. Shahid and M. I. Ullah, "Breast cancer research in Pakistan: A bibliometric analysis," *Sage Open*, vol. 11, no. 3, 2021. doi: 10.1177/21582440211046934.

[4]   A. Yousef, F. Bozkurt, and T. Abdeljawad, "Mathematical modeling of the immune-chemotherapeutic treatment of breast cancer under some control parameters," *Adv. Differ. Equ.*, vol. 2020, 2020, Art. no. 696. doi: 10.1186/s13662-020-03151-5.

[5]   F. B. Yousef, A. Yousef, T. Abdeljawad, and A. Kalinli, "Mathematical modeling of breast cancer in a mixed immune-chemotherapy treatment considering the effect of ketogenic diet," *Eur. Phys. J. Plus*, vol. 135, no. 12, 2020, Art. no. 952. doi: 10.1140/epjp/s13360-020-00991-8.

[6]   A. -K. Vranso West *et al.*, "Division induced dynamics in non-invasive and invasive breast cancer," *Biophys J.*, vol. 112, no. 3, 2017, Art. no. 123A. doi: 10.1016/j.bpj.2016.11.687.

[7]   S. Sapate, S. Talbar, A. Mahajan, N. Sable, S. Desai and M. Thakur, "Breast cancer diagnosis using abnormalities on ipsilateral views of digital mammograms," *Biocybern. Biomed. Eng.*, vol. 40, no. 1, pp. 290–305, 2020. doi: 10.1016/j.bbe.2019.04.008.

[8]   M. J. Yaffe and J. G. Mainprize, "Risk of radiation-induced breast cancer from mammographic screening," *Radiology*, vol. 258, no. 1, pp. 98–105, 2011. doi: 10.1148/radiol.10100655.

[9]   A. A. Khan and A. S. Arora, "Thermography as an economical alternative modality to mammography for early detection of breast cancer," *J. Healthc. Eng.*, vol. 2021, no. 6, pp. 1–8, 2021. doi: 10.1155/2021/5543101.

[10] A. Lubkowska and M. Chudecka, "Thermal characteristics of breast surface temperature in healthy women," *Int. J. Environ. Res. Public Health*, vol. 18, no. 3, pp. 1–11, 2021. doi: 10.3390/ijerph18031097.

[11] J. Amin, M. Sharif, S. L. Fernandes, S. -H. Wang, T. Saba and A. R. Khan, "Breast microscopic cancer segmentation and classification using unique 4-qubit-quantum model," *Microsc. Res. Tech.*, vol. 85, no. 5, pp. 1926–1936, 2022. doi: 10.1002/jemt.24054.

[12] H. G. Zadeh, J. Haddadnia, O. R. Seryasat, and S. M. M. Isfahani, "Segmenting breast cancerous regions in thermal images using fuzzy active contours," *EXCLI J.*, vol. 15, pp. 532–550, Aug. 2016. doi: 10.17179/excli2016-273.

[13] V. Madhavi and C. B. Thomas, "Multi-view breast thermogram analysis by fusing texture features," *Quant. Infrared Thermogr. J.*, vol. 16, no. 1, pp. 111–128, Jan. 2019. doi: 10.1080/17686733.2018.1544687.

[14] M. A. Díaz-Cortés *et al.*, "A multi-level thresholding method for breast thermograms analysis using Dragonfly algorithm," *Infrared Phys. Technol.*, vol. 93, no. 4, pp. 346–361, Sep. 2018. doi: 10.1016/j.infrared.2018.08.007.

[15] P. Kapoor, S. V. A. V. Prasad, and S. Patni, "Image segmentation and asymmetry analysis of breast thermo-grams for tumor detection," *Int. J. Comput. Appl.*, vol. 50, no. 9, pp. 40–45, 2012. doi: 10.5120/7803-0932.

[16] N. Venkatachalam, L. Shanmugam, G. C. Heltin, G. Govindarajan, and P. Sasipriya, "Enhanced seg-mentation of inflamed ROI to improve the accuracy of identifying benign and malignant cases in breast thermogram," *J. Oncol.*, vol. 2021, no. 3, pp. 1–17, 2021. doi: 10.1155/2021/5566853.

[17] L. F. Silva *et al.*, "A new database for breast research with infrared image," *J. Med. Imaging Health Inform.*, vol. 4, no. 1, pp. 92–100, 2014. doi: 10.1166/jmihi.2014.1226.

[18] D. Kusnik and B. Smolka, "Robust mean shift filter for mixed Gaussian and impulsive noise reduction in color digital images," *Sci. Rep.*, vol. 12, no. 1, pp. 1–24, 2022. doi: 10.1038/s41598-022-19161-0.

[19] M. Kalbasi and H. Nikmehr, "Noise-robust, reconfigurable Canny edge detection and its hardware realization," *IEEE Access*, vol. 8, pp. 39934–39945, 2020. doi: 10.1109/ACCESS.2020.2976860.

[20] M. H. Bharati, J. J. Liu, and J. F. MacGregor, "Image texture analysis: Methods and comparisons," *Chemometr. Intell. Lab. Syst.*, vol. 72, no. 1, pp. 57–71, 2004. doi: 10.1016/j.chemolab.2004.02.005.

[21] MathWorks, "Texture analysis using the gray-level co-occurrence matrix (GLCM)," Accessed: Jan. 24, 2024. [Online]. Available: https://www.mathworks.com/

[22] Y. Wang, X. Liao, F. Xiao, H. Zhang, J. Li and M. Liao, "Magnetic resonance imaging texture analysis in differentiating benign and malignant breast lesions of breast imaging reporting and data system 4: A preliminary study," *J. Comput. Assist. Tomogr.*, vol. 44, no. 1, pp. 83–89, 2020. doi: 10.1097/RCT.0000000000000969.

[23] P. Gupta, D. Doermann, and D. DeMenthon, "Beam search for feature selection in automatic SVM defect classification," in *2002 Int. Conf. Pattern Recogniti.*, Quebec City, QC, Canada, 2002, pp. 212–215. doi: 10.1109/ICPR.2002.1048275.

[24] S. Pramanik, D. Bhattacharjee, and M. Nasipuri, "MSPSF: A multi-scale local intensity measurement function for segmentation of breast thermogram," *IEEE Trans. Instrum. Meas.*, vol. 69, no. 6, pp. 2722–2733, 2020. doi: 10.1109/TIM.2019.2925879.

[25] S. Pramanik, S. Ghosh, D. Bhattacharjee, and M. Nasipuir, "Segmentation of breast-region in breast thermogram using arc-approximation and triangular-space search," *IEEE Trans. Instrum. Meas.*, vol. 69, no. 7, pp. 4785–4795, 2020. doi: 10.1109/TIM.2019.2956362.

[26] S. Tello-Mijares, F. Woo, and F. Flores, "Breast cancer identification via thermography image segmentation with a gradient vector flow and a convolutional neural network," *J. Healthc. Eng.*, vol. 2019, pp. 1–13, 2019. doi: 10.1155/2019/9807619.

[27] G. Sayed, M. Soliman, and A. Hassanien, "Bio-inspired swarm techniques for thermogram breast cancer detection," in *Med. Imaging Clin. Appl.: Algorithmic Comput.-Based Approaches*, Cham, Springer International Publishing, 2016, pp. 487–506. doi: 10.1007/978-3-319-33793-7_21.

[28] D. Sathish, S. Kamath, K. Prasad, and R. Kadavigere, "Role of normalization of breast thermogram images and automatic classification of breast cancer," *Vis. Comput.*, vol. 35, no. 1, pp. 57–70, Apr. 2019. doi: 10.1007/s00371-017-1447-9.